

Multi-Scale Investigation of Human Renal Tissue in Three Dimensions

M. Busse¹, S. Ferstl, M. A. Kimm², L. Hehn, K. Steiger, S. Allner, M. Müller, E. Drecoll, T. Bürkner, M. Dierolf³, B. Gleich⁴, W. Weichert, and F. Pfeiffer⁵

Abstract—Histopathology as a diagnostic mainstay for tissue evaluation is strictly a 2D technology. Combining and supplementing this technology with 3D imaging has been proposed as one future avenue towards refining comprehensive tissue analysis. To this end, we have developed a laboratory-based X-ray method allowing for the investigation of tissue samples in three dimensions with isotropic volume information. To assess the potential of our method for micro-morphology evaluation, we selected several kidney regions from three patients with cystic kidney disease, obstructive nephropathy and diabetic glomerulopathy. Tissue specimens were processed using our in-house-developed X-ray eosin stain and investigated with a commercial microCT and our in-house-built NanoCT. The microCT system provided overview scans with voxel sizes of 14.8 μm and the NanoCT was employed for higher resolutions including voxel sizes from 1.4 μm to 210 nm. We present a methodology allowing for a precise micro-morphologic investigation in three dimensions which is compatible with conventional histology. Advantages of our methodology are its versatility with respect to multi-scale investigations, being laboratory-based, allowing for non-destructive imaging and providing isotropic volume information. We believe, that after future developmental work this method might contribute to advanced multi-modal tissue diagnostics.

Index Terms—Microscopic tissue structure, nanoscopic computed tomography, renal pathology, 3D X-ray histology, X-ray staining.

I. INTRODUCTION

IN HISTOPATHOLOGY, a tissue specimen is typically fixed, embedded into paraffin, sectioned by a microtome, stained and analyzed under a light microscope (LM) [1], [2]. To visualize histoarchitecture, the pathologist can choose from a large variety of specific stains. By changing the LM objective and by consulting transmission electron microscopy (TEM), histopathology enables a multi-scale investigation of the tissue

structure in 2D (Fig. 1) [1], [2]. These qualities resulted in histopathology setting the benchmark regarding diagnostic tissue analysis for more than a century.

However, to dive deeper into micro-morphologic evaluation to truly understand tissue architecture, additional 3D information would be desirable. This has prompted the research field of 3D imaging. It allows for tracking and visualizing tissue structures, such as blood vessels, in 3D and provides access to any virtual plane.

Within the field of 3D imaging, a framework of methods based on LM and EM has formed [3], [4], [5], [6], [7], [8]. These methods, however, conventionally involve sectioning or complete destruction of the sample to generate 3D data of a tissue specimen. For instance, to access the glomerular-vascular network in the kidney with scanning electron microscopy (SEM), corrosion casts require in-vivo injection of resin and subsequent dissolution of the surrounding tissue [9], [10]. This procedure renders this approach not suitable in humans. In addition, the 3D data resulting from ablation- or sectioning-based methods often suffer from distortion and alignment artefacts, and the respective ablation or sectioning technique limits the 3D resolution perpendicular to the sectioning plane due to slice thickness [3], [4], [5], [6], [7], [8], [11].

While X-ray computed tomography (CT) enables non-destructive 3D imaging, it conventionally relies on either phase retrieval [12] or staining techniques [13] to achieve adequate tissue contrast. Laboratory-based phase contrast imaging techniques can struggle with reaching the resolutions required to analyze sub-cellular structures [14], can have long exposure times in the order of several tens to hundreds of seconds [15], [16] and generally provide little control over which tissue structures are highlighted [17]. In contrast to that, X-ray staining allows for contrast enhancement of specific cellular structures [18], [19], [20], but represents an additional sample processing step and special care must be taken to avoid compromising the sample structure [11].

We recently introduced a 3D X-ray micromorphology method using X-ray staining. An eosin-based cytoplasm-specific X-ray stain (X-ray eosin stain) combined with propagation-based phase retrieval and an in-house-built, laboratory-based X-ray CT device with resolutions in the 100 nm regime (NanoCT) [21] form the cornerstones of this technique. In previous work, we applied this method to mouse kidney tissue and demonstrated the visualization of sub-cellular details [22]. In a preliminary study analyzing human tissue, we successfully performed a micro-morphological assessment of 3D volumes of renal cell

Manuscript received 1 October 2021; revised 2 December 2021; accepted 7 December 2021. Date of publication 17 October 2022; date of current version 2 December 2022. This work was supported by the European's Union Horizon 2020 Research and Innovation Program through the Marie Skłodowska-Curie Grant H2020-MSCA-IF-2015-703745-CONSALT. (M. Busse, S. Ferstl, W. Weichert, and F. Pfeiffer contributed equally to this work.) (Corresponding author: M. Busse.)

This work involved human subjects or animals in its research. Approval of all ethical and experimental procedures and protocols was granted by the Ethics Committee of the Technical University of Munich, and performed in line with the Declaration of Helsinki.

Please see the Acknowledgment section of this article for the author affiliations.

This article has supplementary downloadable material available at <https://doi.org/10.1109/TMI.2022.3214344>, provided by the authors.

Digital Object Identifier 10.1109/TMI.2022.3214344

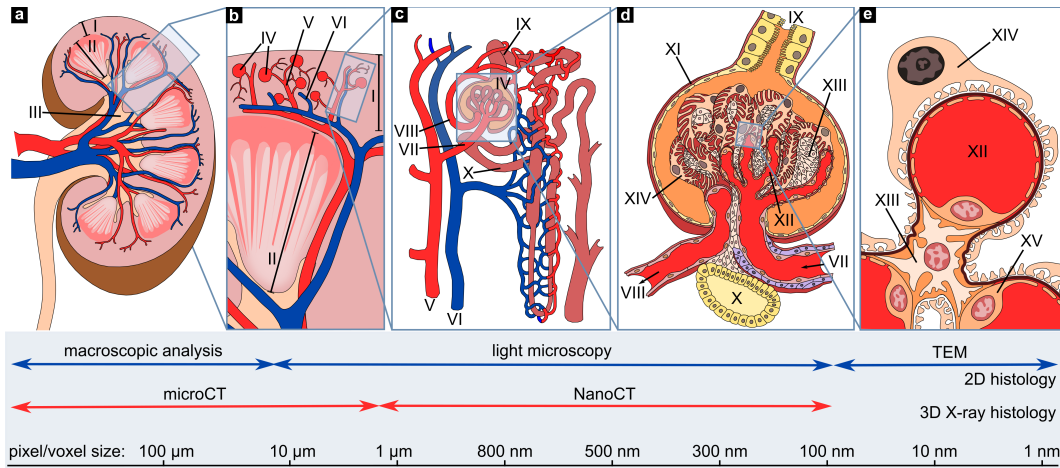


Fig. 1. Schematic overview over the multi-scale kidney anatomy and the resolution range of typical imaging methods along with typical voxel/pixel sizes used in 3D X-ray histology and 2D histology. (a) Overview schematic of a human kidney. (b) Enlarged region indicating the glomerular-vascular network. (c) Schematic of the nephron. (d) Schematic of one glomerulus. (e) Schematic drawing of a capillary within the glomerulus. The assignment of anatomical relevant structures was performed according to D'Agati et al. [1]: Legend: I: cortex, II: medulla, III: pelvis, IV: glomerulus, V: interlobular artery, VI: interlobular vein, VII: afferent arteriole, VIII: efferent arteriole, IX: proximal tubule, X: distal tubule, XI: Bowman's capsule, XII: capillary, XIII: mesangial cell(s), XIV: podocyte with foot processes, XV: fenestrated endothelial cell.

carcinoma [23]. In this context, we further demonstrated compatibility of the X-ray eosin stain with subsequent conventional histological analyses [23]. By measuring samples prepared with TEM-compatible procedures in the NanoCT, we have shown the potential for correlative microscopy with TEM [11].

Here, we want to further explore the benefits of our methodology. We consider contrast, resolution, reliability, versatility, and compatibility with histopathology to be the key aspects in this regard. Thereby, we aim to particularly illustrate the versatility of our method by 3D visualization of a variety of pathologically relevant tissue morphologies on multiple length scales. For a prototypical study, we selected several human tissue specimens presenting non-neoplastic kidney disease.

The kidney plays a central role in a large variety of human diseases and in this context shows diverse micro- and macro-morphological alterations superimposed on a complex basic architecture. Thus, diagnostically evaluating kidney morphologies is highly relevant in the context of various either local or systemic diseases [1], [24], [25].

The hierarchical structures of the kidney span over a wide range of length scales, from the macroscopic regions to the microscopic functional unit, the nephron [1]. To gain a holistic understanding of both, healthy and pathologically altered renal tissue, multi-scale imaging is thus mandatory. On the one hand, rather large tissue volumes need to be investigated to evaluate kidney tissue for detecting diseases such as renal cell carcinoma [26]. Glomerulopathies, on the other hand, require analysis on a cellular level and in some cases even TEM imaging [1], [27], [28]. These characteristics render the kidney an ideal test case for our purposes.

In our study, we acquired high-resolution 3D X-ray CT data of various X-ray eosin-stained human renal tissue specimens exhibiting different pathologies. We performed a comparative evaluation with histological light microscopy images from corresponding regions including a joint interpretation of the X-ray CT and of the histological slides by pathologists from our team.

To account for the various tissue structures, we used a multi-scale approach combining microCT and NanoCT imaging.

The resulting data include volumes ranging from 6 mm edge length down to 150 μm edge length, and effective voxel sizes of 14.8 μm down to 210 nm. These results demonstrate the flexibility of our methodology to perform multi-scale investigations.

On a large volume scale, we performed a scan of cystic kidney tissue. We further present co-registration of microCT and NanoCT data of the same selected tissue region within the tissue specimen. Going towards higher resolutions, we present NanoCT data on tubular morphology and reveal the micro-architecture of the glomerular-vascular network in the human kidney.

In the range of sub-cellular resolutions, we applied advanced CT reconstruction algorithms to investigate a single glomerulus. The respective NanoCT results allowed for detecting the disturbed glomerular tissue architecture. These findings support our methodology as a future promising tool to be used for 3D-multi-scale studies of human pathologies.

II. MATERIALS AND METHODS

A. Experimental Design

To evaluate the potential of our method for histopathology, we selected an organ with a broad morphological diversity and a variety of different pathologies. All samples were resection specimens obtained from the Department of Pathology, Technical University of Munich. The studies were approved by the local ethics committee. We selected several kidney regions from three patients with kidney diseases: Patient A (64 years old, male) was diagnosed with polycystic kidney disease. The resection specimen originated from the cortex region. Patient B (68 years old, female) had tubular degenerations due to an obstruction in the urinary tract. The investigated resection was taken from the transition area from cortex to medulla. Patient C (55 years old, male) was suffering from a post-operative shock combined with long-term diabetes. The resection specimen was of cortical origin. The tissue specimens from the three patients were processed using our in-house-developed X-ray eosin stain and investigated with a commercial microCT and our in-house-built NanoCT.

Thereby, the microCT system was used for overview scans with voxel sizes of $14.8 \mu\text{m}$ and the NanoCT was employed for higher resolutions including voxel sizes from $1.4 \mu\text{m}$ to 210 nm . Pieces of the X-ray eosin-stained tissue specimens were analyzed by conventional histology to provide LM images for comparison with the X-ray CT data.

B. X-Ray Eosin Staining

The Department of Pathology of the Technical University of Munich provided formalin-fixed (4% phosphate-buffered saline formalin solution) tissue fragments from the dissection room. The further sample processing was carried out following the previously described steps [22], [23], [29]. After acidification with 5% (vol/vol) glacial acetic acid in phosphate-buffered saline formalin solution; Alfa Aesar), the tissue specimens were washed with phosphate-buffered saline solution (DPBS without calcium and magnesium) for 1 h. For the eosin staining, the sample was left in eosin Y staining solution (30 % (wt/vol) in distilled water) (Sigma-Aldrich) for 24 h at room temperature. The amount of staining solution was chosen such that the tissue sample was fully covered (volume ranged from 6 to 15 ml for sample sizes of 3 – 5 cm edge length). During that time, the sample container was placed on a horizontal shaking plate at 60 rpm. After the incubation time and removal of excess staining solution, the samples were stored in an ethanol vapor phase of 70 % (vol/vol) ethanol. Prior to imaging the tissue samples were cut into smaller tissue pieces to allow for subsequent sample processing in histology and to visualize the micro-morphological structures.

C. X-Ray microCT: Acquisition

Each of the X-ray eosin-stained tissue specimens was placed in a sample holder in a 70 % (vol/vol) ethanol vapor phase. For the microCT data, shown in Fig. 2a-d, Fig. S1, Fig. S2,¹ 1,601 projections were acquired over an angular range of 360° using the Xradia Versa 500 (Zeiss) at a peak voltage of 50 kV. The 0.39x objective and an exposure time of 2 s were chosen to achieve adequate data quality at an effective voxel size of $14.8 \mu\text{m}$. These settings resulted in a total acquisition time of $\sim 2 \text{ h}$ per CT scan. The chosen parameters ensured optimal transmission values between 0.22 and 0.35 and provided a good signal-to-noise ratio with at least 5000 average counts per pixel within the field of view (FOV) as suggested by the manufacturer.

D. X-Ray microCT: Image Processing, Reconstruction and 3D Visualization

The image processing of all microCT data sets was performed within an in-house developed Python framework. The flat-field normalized projections were corrected to remove ring and intensity fluctuation artefacts. The reconstruction was carried out with a state-of-the-art filtered back-projection algorithm [30] including a center-shift correction based on cross-correlation of anti-posed projections [31] and an angular

projection alignment based on tomoconsistency [32]. The volume renderings of the microCT data were generated with Avizo Fire 8.1 (ThermoFisher Scientific).

E. X-Ray NanoCT: Sample Preparation

The imaging at very high resolutions requires the sample to be very stable over the time of measurement. Critical-point drying (CPD) is a suitable sample preparation method for the tissue samples and their investigation with the NanoCT. Furthermore, the CPD enables the positioning of the tissue sample especially close to the X-ray source to allow for the best possible magnification and imaging result. Based on the microCT data, volumes of interest (VOI) were defined. From these VOIs, samples with an edge length of 0.5-1 mm were extracted and dehydrated in an ethanol series (50, 60, 70, 80, 90, 96, and 100 % (vol/vol) in distilled water) for 1 h each and then critical-point dried (Bal-TEC CPD 030) analogously to previously described protocols [23]. The samples were kept in a desiccator until further use.

F. X-Ray NanoCT: Acquisition

The NanoCT is an in-house-developed laboratory system. It is based on the principle of a shadow microscope and, thereby, does not rely on X-ray or visible light optics for magnification. By combining a nanofocus X-ray source (prototype Nanotube; Excillum) [33] with a single-photon counting detector (PILATUS 300K-W 20 Hz, Dectris) [34] it reaches resolutions down to 100 nm [21]. For the presented data, 1,599 projections, evenly distributed over 360° , were taken at a peak voltage of 60 kV.

The NanoTube allows for calibrating the focal spot size of the electron beam onto the X-ray transmission target. The electron spot sizes which are provided in the following describe the radius or 0.5 FWHM (full-width-at-half-maximum). For the data shown in Fig. 2f-i (patient A) an exposure time of 2 s and an effective voxel size of $\sim 1.4 \mu\text{m}$ was set (electron spot size was 340 nm), which results in a total acquisition time of $\sim 2 \text{ h}$ for the CT scan. Regarding the NanoCT data of Fig. 3 (patient B) the exposure time of 5 s and an effective voxel size of $\sim 430 \text{ nm}$ (electron spot size was 320 nm) led to a total acquisition time of $\sim 4 \text{ h}$ per CT scan. The data set from Fig. 4 (patient C) was taken with an exposure time of 3 s and an effective voxel size of $\sim 890 \text{ nm}$ (electron spot size was 320 nm) in $\sim 2.5 \text{ h}$ per CT scan. To extend the FOV in the vertical direction, multiple CT scans were taken for different vertical positions of the sample and later digitally combined in 3D. Thereby, 3 data sets were taken, which adds up to a total acquisition time of the final data set of $\sim 7.5 \text{ h}$. For the NanoCT data of Fig. 5 (patient C), 7 data sets were acquired at different vertical positions with an exposure time of 8 s, an effective voxel size of $\sim 210 \text{ nm}$ (electron spot size was 360 nm), an acquisition time of $\sim 5 \text{ h}$ per data set during $\sim 35 \text{ h}$.

G. X-Ray NanoCT: Image Processing, Reconstruction and 3D Visualization

All NanoCT data sets were processed and reconstructed using an in-house written Python framework. The flat-field

¹Supporting materials are available in the supporting documents/multimedia tab.

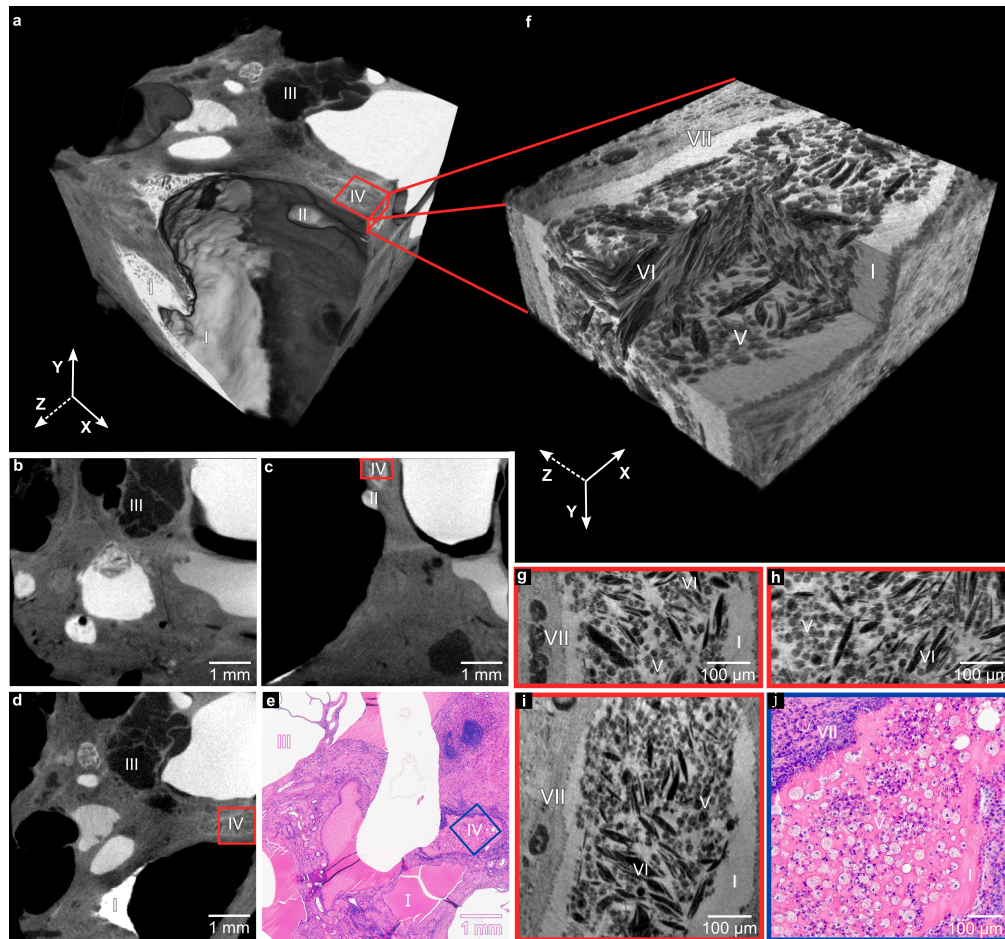


Fig. 2. MicroCT and NanoCT data and histology image of a polycystic kidney specimen (patient A). (a) MicroCT rendering of 5.8 mm x 5.8 mm x 5.5 mm with a VOI marked in red (effective voxel size $\sim 14.8 \mu\text{m}$). (b) – (d) MicroCT slices through the volume shown in (a) along the Cartesian axes: (b) along xy, (c) along yz and (d) along xz. (e) Histological image with a ROI marked in blue. (f) NanoCT rendering of $500 \mu\text{m} \times 500 \mu\text{m} \times 270 \mu\text{m}$ of the VOI indicated in red in (a) (effective voxel size $\sim 1.4 \mu\text{m}$). The viewing angle of the red VOI has been changed here for illustration purposes. (g) – (i) NanoCT slices through the volume shown in (f) along the Cartesian axes: (g) along yz, (h) along xy and (i) along xz. (j) Enlarged histological light microscopy image from the ROI indicated in blue in (e). ROI has been rotated for illustration purposes. Legend: I: amorphous eosinophilic material, II: nodular region in cyst wall, III: multilocular cyst, IV: foam cell aggregate ROI/VOI, V: foam cells, VI: cholesterol crystals, VII: lymphocytic demarcation.

and intensity corrected projections were processed according to Gureyev's approach of edge deblurring [35] using Paganin's method [12] for phase-retrieval. Thereby, the input values were chosen to achieve the maximum edge sharpness, whilst dampening edge-enhancement effects and optimizing the soft-tissue contrast. The resulting projections were reconstructed using a state-of-the-art filtered back-projection algorithm. Prior to reconstruction, a center-shift correction and a projection alignment based on cross-correlation [36] were applied to the NanoCT data presented in Fig. 2 – 5. For the NanoCT data with the smallest effective voxel size of 210 nm (Fig. 5), the detector offset was optimized for each individual projection employing a sparsity metric [11], [37]. The volumes presented in Fig. 4 and Fig. 5 were combined from 3 and 7 sub-volumes, respectively. The alignment of the sub-volumes was carried out with a shift-calculation technique based on cross-correlation. The NanoCT volume renderings, segmentations (Fig. 2 – 5) and movies (Movie S1 – S3) were created with Avizo Fire 8.1 (Thermo Fisher Scientific). The segmentation was intensity-based but performed manually followed by interpolation. An automatic segmentation was not possible due to

the bright erythrocytes within the dark blood vessels and the high degradation state of the tissue.

H. Histology

Remaining tissue fragments after microCT acquisition and after resection of the NanoCT tissue pieces from the X-ray eosin-stained tissue specimens were returned to the Pathology Lab for further analysis. The NanoCT tissue pieces and the remaining tissue shared a resection plane. Following the standard protocols, tissue blocks of around 1 cm - 1.5 cm-edge length were embedded into paraffin and sectioned into $3\text{-}\mu\text{m}$ thick slices using a microtome (Leica). A distance of $100\text{--}300 \mu\text{m}$ must be assumed from the investigated NanoCT piece to the histological slides shown. This considers that initial slides might be discarded, e.g. due to inclined embedding. The distance ensures the presence of corresponding micro-structures seen in the NanoCT volume. The histological slides were deparaffinized, rehydrated and counter stained with Mayer's hematoxylin (Morphisto) according to the manufacturer's protocol. The resulting histological images were acquired with a Zeiss microscope (AxioImager II,

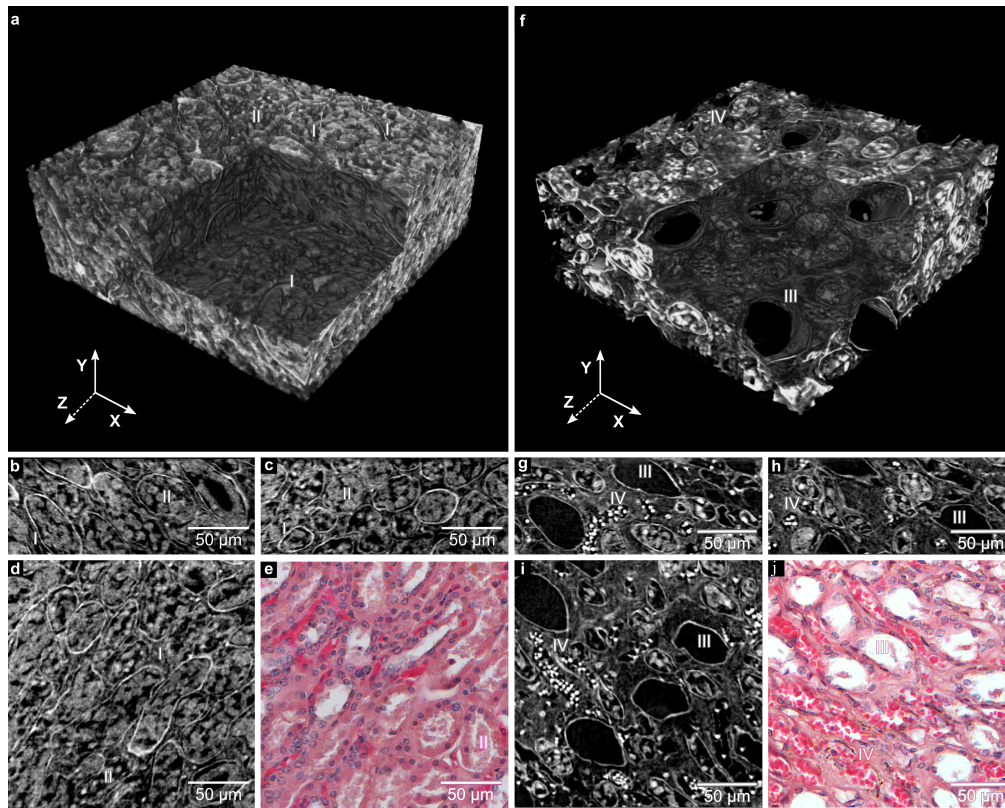


Fig. 3. Two sets of NanoCT data and histology image of altered renal tubular tissue showing different degrees of tubular degradation (patient B). (a) First NanoCT rendering of $206 \mu\text{m} \times 206 \mu\text{m} \times 80 \mu\text{m}$ (effective voxel size $\sim 480 \text{ nm}$) presenting tubuli with intraluminal cell debris. (b)–(d) NanoCT slices through the volume shown in (a) along the Cartesian axes: (b) along xy, (c) along yz and (d) along xz. (e) Histological image with hematein counterstain. (f) Second rendering of $206 \mu\text{m} \times 206 \mu\text{m} \times 80 \mu\text{m}$ (effective voxel size $\sim 480 \text{ nm}$) showing tubular atrophy and tubular dilation. (g)–(i) NanoCT slices through the volume shown in (f) along the Cartesian axes: (g) along xy, (h) along yz and (i) along xz. (j) Histological image with hematein counterstain. Legend: I: interstitial connective tissue, II: tubuli with intraluminal cell debris, III: tubular atrophy and tubular dilation, IV: erythrocytes in peritubular ectatic capillaries.

Carl Zeiss, Germany) equipped with AxioVision software (version 4.7, Carl Zeiss, Germany). For the light microscopy image in Fig. 2e, a 5x objective (0.17 NA) was used. For the images shown in Fig. 2k, Fig. 3e, Fig. 3k, and Fig. 5f a 20x objective (0.5 NA) and for Fig. 4f a 10x objective (0.3 NA) was used. For all objectives the resolution is limited by the effective pixel size of the image after magnification with $2.075 \mu\text{m}/\text{pixel}$, $1.029 \mu\text{m}/\text{pixel}$, and $516 \text{ nm}/\text{pixel}$, respectively.

III. RESULTS

A. Cystic Kidney Disease

A typical kidney disease exhibiting hierarchical structures on a large range of length scales is cystic kidney disease. Here, we investigated specific areas of polycystic kidney with microCT and further extracted a smaller volume of interest (VOI) for assessments on a cellular level using the NanoCT.

Fig. 2 presents the resulting microCT and NanoCT data along with the corresponding histology images. Eosinophilic areas appeared bright in the X-ray CT data and pink in the histology images, since both, the applied X-ray stain and the histological stain contain eosin. Eosinophilic structures in histopathology characteristically have a high protein content, such as the cell cytoplasm or erythrocytes.

The microCT data in Fig. 2 largely reflected the tissue morphology visible in the histological slide, such as multilocular cysts and areas where potential inflammatory infiltrates were

present. During the analyses, a smaller VOI was identified containing relevant underlying sub-structures beyond the resolution limit of the used microCT.

For a precise assessment of the micro-morphology, i.e., to determine whether the VOI was representing a papillary renal cell carcinoma or simply a foam cell aggregate, the VOI was cut from the tissue cube and further data was acquired using the NanoCT. Based on the NanoCT visualizations, we were able to identify the volume as a foam cell aggregate. In the histological slide in Fig. 2e, the corresponding region of interest (ROI, marked in blue) displayed most of the structures visible in the NanoCT images (Fig. 2f-i), such as foam cells and lymphocytic demarcation. Cholesterol crystals, which were dissolved during paraffin embedding, could not be detected in the histological image, while being clearly discernible in the NanoCT data.

It was possible to assign the NanoCT volume (Fig. 2f) to the indicated VOI in the microCT data (Fig. 2a, red box and Movie S1²), which demonstrated targeted correlative multi-scale imaging using high-resolution X-ray CT.

B. Tubular Morphology

Altered tubular morphology was assessed in a tissue specimen of a patient suffering from an obstruction of the urinary tract (patient B). In this case, the microCT data yielded only

²Supporting materials are available in the supporting documents/multimedia tab.

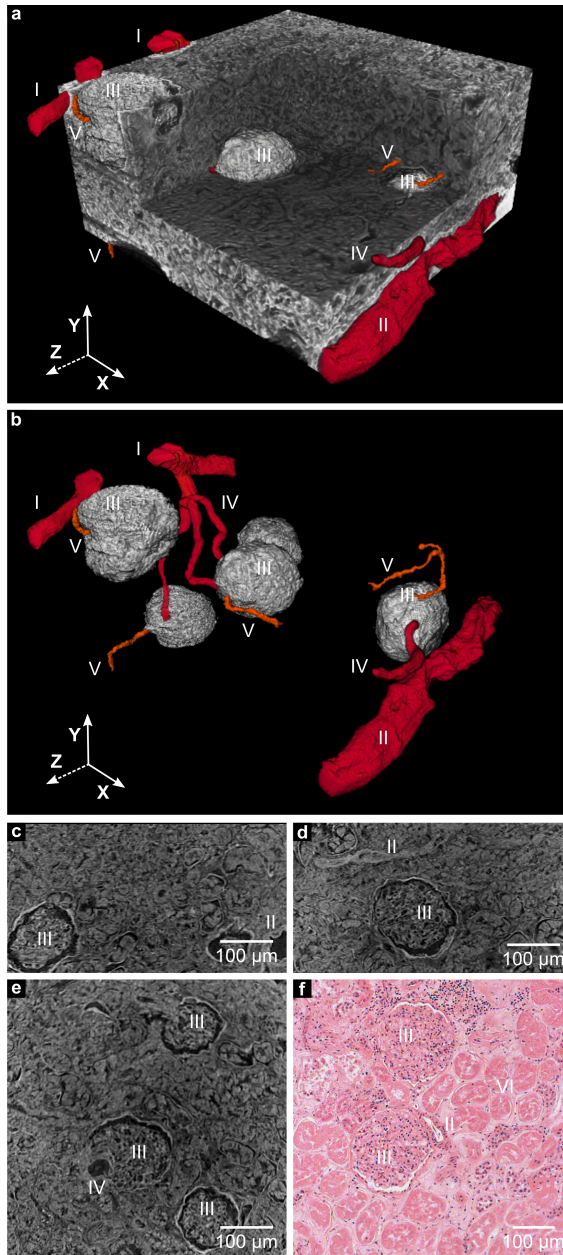


Fig. 4. NanoCT data and histology image of a diabetic kidney with superimposed shock from the cortex region (patient C). (a) NanoCT volume rendering of a volume of $500\ \mu\text{m} \times 500\ \mu\text{m} \times 250\ \mu\text{m}$ of the tissue with the glomeruli and the blood vessels modelled in 3D (effective voxel size $\sim 890\ \text{nm}$). (b) 3D rendering of the glomeruli, the interlobular artery, and the associated arterioles without the surrounding tissue within the volume shown in (a). (c) – (e) NanoCT slices through the volume shown in (a) along the Cartesian axes: (c) along xy , (d) along yz and (e) along xz . (f) Histological image with hematein counter staining. Legend: I: Interlobular artery, II: blood vessel with thickened vascular wall, III: renal corpuscle with thickened Bowman's capsule, IV: dilated afferent arteriole, V: efferent arteriole, VI: tubular necrosis.

little information (Fig. S1²). Here, solely a blood vessel could be discerned, and tubular micro-morphology was not further assessable.

Therefore, we resected various VOIs for further NanoCT investigations, whereby two NanoCT data sets were particularly interesting. The selected NanoCT data (Fig. 3) reflected tubular morphologies reminiscent of varying degrees of tubular alterations in the context of the underlying disease, which

could also be seen in the corresponding histological images. It thus enabled us to distinguish between different degrees of tubular degradation.

Particularly striking were the bright erythrocytes in ectatic peritubular capillaries seen in the X-ray data of Fig. 3e-i. The brightness of the erythrocytes originated from a high protein content resulting in a high eosin concentration, and thus a pink appearance in the light microscopy image. Furthermore, the tubular walls appear highlighted in the NanoCT slices compared to the histological images. This is due to Paganin's method [12] of propagation-based phase retrieval. As such the tubular walls must have a considerably higher tissue density compared to the neighboring tissue and are therefore highlighted. Due to the chosen standard H&E staining for the histological slides the tubular walls are not highlighted explicitly here and display an additional feature when using the NanoCT for whole tissue imaging.

C. 3D Investigation of the Glomerular-Vascular Network

Apart from the tubular network, we were particularly interested in the glomerular-vascular network as an essential part of the nephron (Fig. 1). MicroCT data was again of little benefit for analyzing these structures (Fig. S2³).

Thus, an overview NanoCT dataset was taken of a tissue specimen from a diabetes patient with a superimposed acute shock (patient C). The resulting NanoCT images (Fig. 4) revealed multiple glomeruli and their associated vasculature and tubular structure. The NanoCT slices displayed a tissue architecture well comparable to the histology image. The micro-morphologic analysis yielded typical shock indicators, such as dilated blood vessels but also typical diabetic changes such as thickened vascular walls and a thickened Bowman's capsule surrounding the renal corpuscles. By tracking the blood vessels in 3D, we were able to segment the interlobular artery and beyond that the afferent arterioles, which connect the artery with the glomeruli, and the efferent arterioles. The 3D renderings in Fig. 4 and Movie S2³ illustrate how the NanoCT data provides 3D information of both, the glomerular-vascular system, and the surrounding tissue simultaneously.

D. 3D Investigation of Glomerulopathies

Having gained an overview over a network of glomeruli, we proceeded to higher resolutions to analyze a single glomerulus. The glomerulus represents the central filtering unit of the kidney and certain glomerulopathies lead to end-stage renal disease [27]. The diagnosis of glomerulopathies involves cellular level investigations and requires sometimes TEM imaging [1], [27], [28]. Thus, we acquired NanoCT data of a tissue piece containing one glomerulus from the same patient (patient C) with a voxel size of $210\ \text{nm}$ (Fig. 5). To reduce blurring due to drifts and mechanical instabilities at these high resolutions, an advanced alignment algorithm for CT reconstruction was devised [11]. The resulting NanoCT slices allowed for an accurate analysis of the glomerular morphology. Due to the X-ray eosin stain, the NanoCT slices map the

³Supporting materials are available in the supporting documents/multimedia tab.

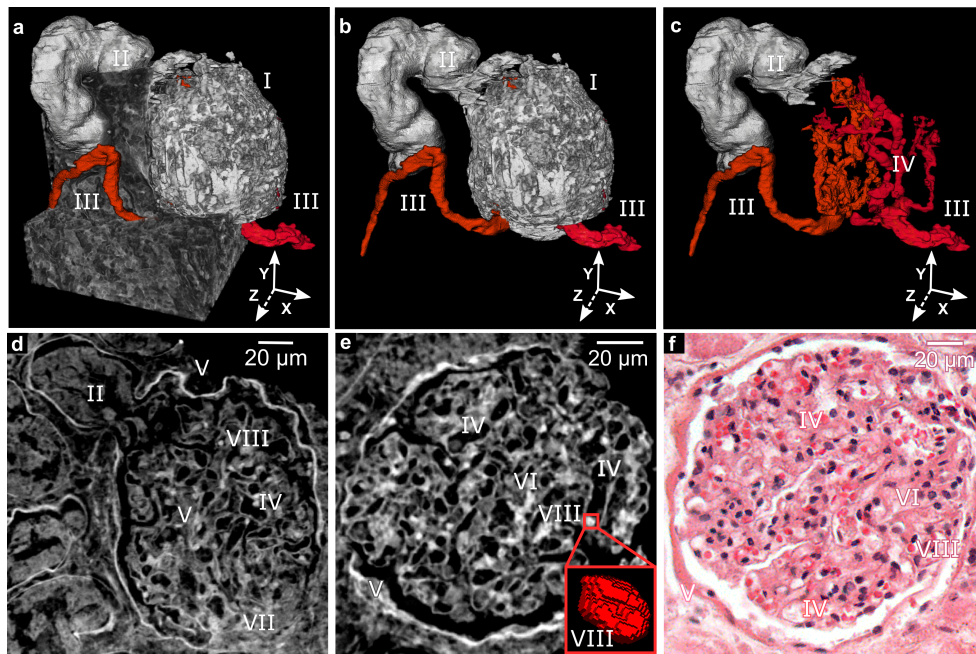


Fig. 5. NanoCT data and histological image of a single partially sclerotic glomerulus (effective voxel size ~ 210 nm) (patient C). (a) NanoCT rendering of $122 \mu\text{m} \times 156 \mu\text{m} \times 170 \mu\text{m}$ with the renal corpuscle, the arterioles and the proximal tubule modelled. (b) 3D model from (a) without surrounding tissue. (c) 3D model from (b) with parts of the capillaries modelled. (d) NanoCT slice through the volume shown in (a) along the xy Cartesian axes. (e) NanoCT slice through the volume shown in (a) along the xz Cartesian axes with a ROI containing an erythrocyte marked in red and an enlarged 3D rendering of the respective erythrocyte. (f) Histological image with hematein counter staining. Legend: I: renal corpuscle, II: proximal tubule, III: afferent/efferent arteriole, IV: capillaries with irregular dilated shape, V: thickened Bowman's capsule, VI: diffuse mesangial thickening, VII: nodular mesangial thickening, VIII: erythrocyte.

eosin distribution within the tissue similar to the histology image. The tissue contrast benefited significantly from the propagation-based phase retrieval enabled through the small voxel sizes due to the concept of the NanoCT. As the NanoCT resembles a shadow microscope with a large cone beam angle, the effective propagation distance is directly linked to the effective voxel size. To achieve low noise levels / high photon counts, the source-detector distance was minimized. Consequently, structures such as the thickened Bowman's capsule were particularly highlighted.

The assessment of the high-resolution 2D NanoCT slices revealed a diffuse and nodular glomerulosclerosis with mesangial thickening. These are typical long-term effects of diabetes mellitus. A nodular mesangial thickening was only visible in the NanoCT slice in Fig. 5d, but not in the NanoCT slice of Fig. 5e nor the corresponding histological image (Fig. 5f).

Cell nuclei in the proximal tubules appeared as slightly darker disks in the NanoCT slices. In contrast to that, erythrocytes mostly appeared as bright disks in the NanoCT slices. A 3D rendering of one erythrocyte (Fig. 5e, red ROI), however, hinted on the characteristic oval biconcave disk-shape. The 3D rendering is displayed without any voxel interpolations creating a step-like surface to illustrate the true voxel resolution. Beyond that, the NanoCT allowed for 3D modelling of the glomerulus, its arterioles, the proximal tubules, a VOI of surrounding tissue (Fig. 5, Movie S3⁴) and even the capillaries inside the glomerulus.

IV. DISCUSSION

In our study, we analyzed a variety of pathologies throughout different kidney regions and diseases. We acquired X-ray CT data of vastly varying volumes with edge lengths ranging from ~ 6 mm to $\sim 150 \mu\text{m}$. To address each of these pathologies, we adjusted the voxel size from $14.8 \mu\text{m}$ down to 210 nm. This was feasible due to the concept of the NanoCT which allows for continuously adjusting the field-of-view (FOV) and effective voxel size at relatively short acquisition times.

By combining a commercial microCT and our in-house developed NanoCT, we demonstrated targeted multi-scale investigation. We employed the microCT system to define a VOI, which we resected and further studied with higher resolutions using the NanoCT.

When it comes to accurately capturing the characteristic tissue structure, there are two basic requirements: adequate tissue contrast and sufficient resolutions.

Regarding the tissue contrast, histopathology employs specific histological stains to highlight the relevant tissue structures. Our method combines the X-ray eosin stain with propagation-based phase contrast. Due to the X-ray eosin stain, we obtain a 3D X-ray absorption map, analogous to the pink eosin distribution known from histology. Beyond that, propagation-based phase retrieval provides a boost in soft-tissue contrast, which especially serves as a highlight for membranes, such as tubular or vascular walls and the glomerular Bowman's capsule. This could be particularly useful for studying glomerulopathies, since our method can visualize both, the mesangial thickening, due to the X-ray

⁴Supporting materials are available in the supporting documents/multimedia tab.

eosin stain, and the thickened Bowman's capsule, using phase effects.

In all tissue samples investigated so far [22], [23], [29], the acidification step carried out as part of the X-ray eosin staining protocol never had an effect on the morphology, so we are confident that it also did not alter the biopsy samples investigated within this study. However, it still needs to be explored how this staining method is affecting potential acid-sensitive structures such as calcium oxalate crystals, as none were present in our samples (confirmed by absorption-based microCT prior to staining). Nonetheless, it should be pointed out that the acid is only present with 5 vol-% and furthermore belongs to the mild acids compared to inorganic acids such as hydrochloric acid. These aspects should minimize the risk of morphological impacts.

The spatial resolution represents the second fundamental condition to adequately visualize tissue. In previous work, we demonstrated a resolution limit of the NanoCT of ~ 100 nm [21]. While it is challenging to determine the actual image resolution of the NanoCT data in this work, it is evident that the images provide a detail level comparable to the corresponding histology images. At voxel sizes around 200 nm, drifts and mechanical instabilities may cause substantial blurring artefacts in the reconstructed CT data. This problem was solved by an advanced alignment algorithm based on a sparsity metric, which corrects positional shifts for every projection image individually [11], [37]. As a result, the NanoCT data in Fig. 5 provides a highly detailed representation of a glomerulus, where it is even possible to track single capillaries inside the glomerulus and reproduce the characteristic biconcave shape of single erythrocytes.

Fulfilling these two criteria, the presented CT results adequately reproduce the tissue morphology as shown by corresponding histologies and thereby enable an accurate micro-morphological assessment. The cholesterol crystals in the foam cell aggregate, for instance, are even better reproduced in the NanoCT images than in the histological slide, since tissue processing for histology washes out these elements. Our method enables to evaluate different degrees of tubular alterations and to detect pathologies affecting single glomeruli.

Apart from these high-performance characteristics for an imaging modality, our method offers further advantages through 3D assessment. Regarding the cystic kidney case, our microCT data allows for an accurate recapitulation of the complex architecture and for the detection of ROIs which could be evaluated further.

When studying the glomerular-vascular network, tracking the blood vessels in 3D provided us with the information to assign the afferent and efferent arterioles for each glomerulus and to identify and image the interlobular artery. Subsequently, we were able to transfer this additional knowledge back to the 2D NanoCT slices. This is an excellent example of how 3D imaging may be aligned with 2D data.

Similar 3D representations of the glomerular-vascular system, as shown in Fig. 4, are known from corrosion cast imaging [9], [10]. In contrast to corrosion cast imaging, however,

our method can visualize both, the glomerular-vascular system and the surrounding tissue.

Another advantage of 3D X-ray is that any arbitrary spatial plane can be analyzed resulting in a multiplication of available information. This is especially advantageous, if the tissue exhibits different morphologies in different spatial planes and is exemplified in our study of a glomerulus. Here, a nodular mesangial thickening was evident only in one of the two (and potentially many additional) orthogonal NanoCT slices.

The compatibility of the NanoCT and TEM has already been demonstrated in previous work [11]. TEM imaging is consulted for certain cases of glomerulopathies. Thus, combining both methods in the future might become a particularly powerful tool for defining VOIs in certain planes by X-ray for further targeted TEM investigation and, thus, allow for a more precise morphological assessment.

Moreover, our methodology is compatible with subsequent clinical histological investigations such as the H&E and fuchsin-based staining procedures [23]. As shown, it is possible to study a sample with conventional histology after applying the X-ray eosin stain. However, up until now, we mostly use CPD to prepare the samples for NanoCT imaging. Thus, it is still left for us to explore whether CPD samples can be processed to allow subsequent paraffin embedding and thereby reach full compatibility with histology.

To conclude, our method fulfils the essential requirements contrast, resolution and reliability to allow for a precise micro-morphological investigation. It offers a multitude of benefits through non-destructive imaging and isotropic volume information. It is laboratory-based and mostly compatible with routine diagnostic histology and TEM imaging. Multi-scale CT imaging on the microscopic and nanoscopic level can provide additional information that might close the gap between LM and EM techniques. We believe, that with further developmental work this method holds the capability of contributing to advanced and precise multi-modality tissue analytics.

APPENDIX

The data that support the findings of this study are available on request from the corresponding author M. Busse. The data are not publicly available due to them containing information that could compromise patient privacy.

ACKNOWLEDGMENT

The authors thank Irina Eskina for technical support.

M. Busse and M. Dierolf are with the Chair of Biomedical Physics, Department of Physics, School of Natural Sciences and the Munich Institute of Biomedical Engineering, Technical University of Munich, 85748 Garching, Germany (e-mail: madleen.busse@tum.de; martin.dierolf@tum.de).

S. Ferstl was with the Chair of Biomedical Physics, Department of Physics, School of Natural Science and the Munich Institute of Biomedical Engineering, Technical University of Munich, 85748 Garching, Germany. She is now with Veridos GmbH, 81677 Munich, Germany (e-mail: simone.ferstl@veridos.com).

M. A. Kimm was with the Department of Diagnostic and Interventional Radiology, School of Medicine, Klinikum rechts der Isar, Technical University of Munich, 81675 Munich, Germany. She is now with the Laboratory for Experimental Radiology, Clinic and Polyclinic for Radiology, Klinikum Großhadern, Ludwig-Maximilian-University Munich, 81377 Munich, Germany (e-mail: melanie.kimm@med.uni-muenchen.de).

L. Hehn was with the Chair of Biomedical Physics, Department of Physics, School of Natural Sciences and the Munich Institute of Biomedical Engineering, Technical University of Munich, 85748 Garching, Germany. He is now with Brainlab AG, 81829 Munich, Germany (e-mail: lorenz.hehn.tum@outlook.com).

K. Steiger is with the Department of Pathology, School of Medicine, Klinikum rechts der Isar, Technical University of Munich, 81675 Munich, Germany (e-mail: katja.steiger@tum.de).

S. Allner was with the Chair of Biomedical Physics, Department of Physics, School of Natural Sciences and the Munich Institute of Biomedical Engineering, Technical University of Munich, 85748 Garching, Germany. He is now with MITOS GmbH, 85748 Garching, Germany (e-mail: sebastian.allner@mitos.de).

M. Müller was with the Chair of Biomedical Physics, Department of Physics, School of Natural Sciences and the Munich Institute of Biomedical Engineering, Technical University of Munich, 85748 Garching, Germany. He is now with SCANLAB GmbH, 82178 Puchheim, Germany (e-mail: mark.mueller222@gmail.com).

E. Drecoll was with the Department of Pathology, School of Medicine, Klinikum rechts der Isar, Technical University of Munich, 81675 Munich, Germany. She is now with the Institute for Pathology, Labor Potsdam, 14467 Potsdam, Germany (e-mail: enken@drecoll.net).

T. Bürkner was with the Chair of Biomedical Physics, Department of Physics, School of Natural Sciences and the Munich Institute of Biomedical Engineering, Technical University of Munich, 85748 Garching, Germany. He is now with Radiotherapy Ingolstadt, 85049 Ingolstadt, Germany (e-mail: t.buerkner@t-online.de).

B. Gleich is with the Munich Institute of Biomedical Engineering, Technical University of Munich, 85748 Garching, Germany (e-mail: gleich@tum.de).

W. Weichert is with the Department of Pathology, School of Medicine, Klinikum rechts der Isar, Technical University of Munich, 81675 Munich, Germany, and also with the German Cancer Consortium (DKTK), Partner Site Munich, 80336 Munich, Germany (e-mail: wilko.weichert@tum.de).

F. Pfeiffer is with the Chair of Biomedical Physics, Department of Physics, School of Natural Sciences, Munich Institute of Biomedical Engineering and Institute for Advanced Study, Technical University of Munich, 85748 Garching, Germany, and also with the Department of Diagnostic and Interventional Radiology, School of Medicine, Klinikum rechts der Isar, Technical University of Munich, 81675 Munich, Germany (e-mail: franz.pfeiffer@tum.de).

REFERENCES

- [1] V. D. D'Agati, C. J. Jenette, and F. G. Silva, *Atlas of Nontumor Pathology—Non-Neoplastic Kidney Diseases*, 1st ed. Rockville, MD, USA: American Registry of Pathology, 2005.
- [2] K. S. Survana, C. Layton, and J. D. Bancroft, *Bancroft's Theory and Practice of Histological Techniques*, 7th ed. Amsterdam, The Netherlands: Elsevier, 2012.
- [3] A. Andreasen, A. M. Drewes, J. E. Assentoft, and N. E. Larsen, "Computer-assisted alignment of standard serial sections without use of artificial landmarks. A practical approach to the utilization of incomplete information in 3-D reconstruction of the hippocampal region," *J. Neurosci. Methods*, vol. 45, no. 3, pp. 199–207, Dec. 1992.
- [4] W. Denk and H. Horstmann, "Serial block-face scanning electron microscopy to reconstruct three-dimensional tissue nanostructure," *PLoS Biol.*, vol. 2, no. 11, pp. 1901–1909, Oct. 2004.
- [5] T. J. Mohun and W. J. Weninger, "Imaging heart development using high-resolution episcopic microscopy," *Current Opinion Genet. Develop.*, vol. 21, no. 5, pp. 573–578, Oct. 2011.
- [6] M. S. Braverman and I. M. Braverman, "Three-dimensional reconstructions of objects from serial sections using a microcomputer graphics system," *J. Invest. Dermatol.*, vol. 86, no. 3, pp. 290–294, Mar. 1986.
- [7] A. Odgaard, K. Andersen, F. Melsen, and H. J. G. Gundersen, "A direct method for fast 3-dimensional serial reconstruction," *J. Microsc.*, vol. 159, no. 3, pp. 335–342, Sep. 1990.
- [8] W. J. Weninger, S. Meng, J. Streicher, and G. B. Müller, "A new episcopic method for rapid 3-D reconstruction: Applications in anatomy and embryology," *Anatomy Embryol.*, vol. 197, no. 5, pp. 341–348, Apr. 1998.
- [9] F. E. Hossler and J. E. Douglas, "Vascular corrosion casting: Review of advantages and limitations in the application of some simple quantitative methods," *Microsc. Microanalysis*, vol. 7, no. 3, pp. 253–264, May 2001.
- [10] D. Casellas and A. Mimran, "Shunting in renal microvasculature of the rat: A scanning electron microscopic study of corrosion casts," *Anatomical Rec.*, vol. 201, no. 2, pp. 237–248, Oct. 1981.
- [11] S. Ferstl et al., "Nanoscope X-ray tomography for correlative microscopy of a small meiofaunal sea cucumber," *Sci. Rep.*, vol. 10, no. 1, pp. 1–12, Mar. 2020.
- [12] D. Paganin, S. Mayo, T. E. Gureyev, P. R. Miller, and S. W. Wilkins, "Simultaneous phase and amplitude extraction from a single defocused image of a homogeneous object," *J. Microsc.*, vol. 206, no. 1, pp. 33–40, Apr. 2002.
- [13] B. D. Metscher, "Micro CT for comparative morphology: Simple staining methods allow high-contrast 3D imaging of diverse non-mineralized animal tissues," *BMC Physiol.*, vol. 9, no. 1, p. 11, Jun. 2009.
- [14] M.-C. Zdora et al., "X-ray phase imaging with the unified modulated pattern analysis of near-field speckles at a laboratory source," *Appl. Opt.*, vol. 59, no. 8, pp. 2270–2275, Mar. 2020.
- [15] W. Vågberg, D. H. Larsson, M. Li, A. Arner, and H. M. Hertz, "X-ray phase-contrast tomography for high-spatial-resolution zebrafish muscle imaging," *Sci. Rep.*, vol. 5, no. 1, pp. 1–7, Nov. 2015.
- [16] M. Töpperrwien, A. Markus, F. Alves, and T. Salditt, "Contrast enhancement for visualizing neuronal cytoarchitecture by propagation-based X-ray phase-contrast tomography," *NeuroImage*, vol. 199, pp. 70–80, Oct. 2019.
- [17] M. Töpperrwien, T. R. Doepfner, B. Zechmeister, M. Bähr, and T. Salditt, "Multiscale X-ray phase contrast tomography in a mouse model of transient focal cerebral ischemia," *Biomed. Opt. Exp.*, vol. 10, no. 1, pp. 92–103, Dec. 2018.
- [18] M. Müller et al., "Nucleus-specific X-ray stain for 3D virtual histology," *Sci. Rep.*, vol. 8, pp. 1–10, Dec. 2018.
- [19] H. Jahn et al., "Evaluation of contrasting techniques for X-ray imaging of velvet worms (Onychophora)," *J. Microsc.*, vol. 270, pp. 343–358, Feb. 2018.
- [20] M. Saccamano et al., "Synchrotron inline phase contrast μ CT enables detailed virtual histology of embedded soft tissue samples with and without staining," *J. Synchrotron Radiat.*, vol. 25, no. 4, pp. 1153–1161, 2018.
- [21] M. Müller et al., "Myoanatomy of the velvet worm leg revealed by laboratory-based nanofocus X-ray source tomography," *Proc. Nat. Acad. Sci. USA*, vol. 114, no. 47, pp. 12378–12383, Nov. 2017.
- [22] M. Busse et al., "Three-dimensional virtual histology enabled through cytoplasm-specific X-ray stain for microscopic and nanoscopic computed tomography," *Proc. Nat. Acad. Sci. USA*, vol. 115, no. 10, pp. 2293–2298, Jan. 2018.
- [23] S. Ferstl et al., "Revealing the microscopic structure of human renal cell carcinoma in three dimensions," *IEEE Trans. Med. Imag.*, vol. 39, no. 5, pp. 1494–1500, Nov. 2019.
- [24] J. L. Gross, M. J. de Azevedo, S. P. Silveiro, L. H. Canani, M. L. Caramori, and T. Zelmanovitz, "Diabetic nephropathy: Diagnosis, prevention, and treatment," *Diabetes Care*, vol. 28, no. 1, pp. 164–176, Jan. 2005.
- [25] T. W. C. Tervaert et al., "Pathologic classification of diabetic nephropathy," *J. Amer. Soc. Nephrol.*, vol. 21, no. 4, pp. 556–563, Apr. 2010.
- [26] A. Schwarz, S. Vatandaslar, S. Merkel, and H. Haller, "Renal cell carcinoma in transplant recipients with acquired cystic kidney disease," *Clin. J. Amer. Soc. Nephrol.*, vol. 2, no. 4, pp. 750–756, Jul. 2007.
- [27] V. D. D'Agati, F. J. Kaskel, and R. J. Falk, "Focal segmental glomerulosclerosis," *New England J. Med.*, vol. 365, pp. 2398–2411, Dec. 2011.
- [28] W. L. Lai et al., "Membranous nephropathy: A review on the pathogenesis, diagnosis, and treatment," *J. Formosan Med. Assoc.*, vol. 114, no. 2, pp. 102–111, Feb. 2015.
- [29] M. Busse et al., "3D imaging of soft-tissue samples using an X-ray specific staining method and nanoscopic computed tomography," *J. Vis. Exp.*, vol. 152, article no. e60251, Oct. 2019.
- [30] A. Fehringer, T. Lasser, I. Zanette, P. B. Noël, and F. Pfeiffer, "A versatile tomographic forward and back projection approach on Multi GPUs," *Proc. SPIE*, vol. 9034, Mar. 2014, Art. no. 90344F.
- [31] V. Patel, R. N. Chityala, K. R. Hoffmann, C. N. Ionita, D. R. Bednarek, and S. Rudin, "Self-calibration of a cone-beam micro-CT system," *Med. Phys.*, vol. 36, no. 1, pp. 48–58, Jan. 2009.
- [32] M. Guizar-Sicairos, J. J. Bohn, K. Mader, A. Diaz, A. Menzel, and O. Bunk, "Quantitative interior X ray nanotography by a hybrid imaging technique," *Optica*, vol. 2, no. 3, pp. 259–266, Mar. 2015.
- [33] F. Nachtrab et al., "Development of a Timepix based detector for the NanoXCT project," *J. Instrum.*, vol. 10, Nov. 2015, Art. no. C11009.
- [34] P. Kraft et al., "Performance of single-photon-counting PILATUS detector modules," *J. Synchrotron Radiat.*, vol. 16, no. 3, pp. 368–375, May 2009.
- [35] T. E. Gureyev, A. W. Stevenson, I. Y. Nesterets, and S. W. Wilkins, "Image deblurring by means of defocus," *Opt. Commun.*, vol. 240, nos. 1–3, pp. 81–88, Oct. 2004.
- [36] D. Gürsoy et al., "Rapid alignment of nanotomography data using joint iterative reconstruction and reprojection," *Sci. Rep.*, vol. 7, pp. 1–12, Sep. 2017.
- [37] L. Hehn, S. Tilley, F. Pfeiffer, and J. W. Stayman, "Blind deconvolution in model-based iterative reconstruction for CT using a normalized sparsity measure," *Phys. Med. Biol.*, vol. 64, no. 21, Oct. 2019, Art. no. 215010.